Multiresolution Dynamic Mode Decomposition (mrDMD) of Elastic Waves for Damage Localisation in Piezoelectric Ceramic

NUR M. M. KALIMULLAH[ID]1**, AMIT SHELKE**[1]**, AND ANOWARUL HABIB**[ID]2
[1]Department of Civil Engineering, Indian Institute of Technology Guwahati, Guwahati, Assam 781039, India
[2]Department of Physics and Technology, UiT The Arctic University of Norway, 9019 Tromsø, Norway

Corresponding author: Anowarul Habib (anowarul.habib@uit.no)

ABSTRACT The performance of piezoelectric sensors deteriorated due to the presence of defect, delamination, and corrosion that needed to be diagnosed for the effective implementation of the structural health monitoring (SHM) framework. A novel experimental approach based on Coulomb coupling is devised to visualise the interaction of ultrasonic waves with microscale defects in the Lead Zirconate Titanate (PZT). Multiresolution dynamic mode decomposition (mrDMD) technique in conjunction with image registration, and Kullback Leibler (KL) divergence is utilised to diagnose and localise the surface defect in the PZT. The mrDMD technique extracts the spatiotemporal coherent mode and provides an equation-free architecture to reconstruct underlying system dynamics. Additionally, due to the strong connection between mrDMD and Koopman operator theory, the proposed technique is well suited to resolve the nonlinear and dispersive interaction of elastic waves with boundaries and defects. The mrDMD sequentially decomposes the three-dimensional spatiotemporal data into low and high frequency modes. The spectral modes are sensitive to defects based on the scaling of wavelength with the size of the defect. The error due to offset and distortion was minimised with ad hoc image registration technique. Further, localisation and quantification of defect are performed by evaluating the distance metric of the probability distribution of coherent data of mrDMD acquired from healthy and defected samples. In the arena of big-data that is ubiquitous in SHM, the paper demonstrates an efficient damage localisation algorithm that explores the nonlinear system dynamics using spectral multi-mode resolution techniques by sensitising the damage features.

INDEX TERMS Damage detection, lead zirconate titanate, multiresolution dynamic mode decomposition, piezoelectric ceramic, structural health monitoring.

I. INTRODUCTION

In recent times, Lead Zirconate Titanate, also known as PZT, has emerged as the preferred choice for excitation of ultrasonic waves for a wide variety of applications. The notable aspects of PZT are wideband spectral response with negligible mass, ease in integration, physical robustness, lower power consumption, and economical benefits. The PZT ceramics play a vital role in several industrial and military applications, such as optoelectronics, telecommunication, biomedical devices, actuators, energy harvesting devices, and structural health monitoring (SHM) [1]–[5]. SHM focuses on diagnostic, etiognosis, and prognosis for improving the

reliability and operational life of mechanical and aerospace structures [6], [7]. SHM can be broadly classified into two main categories, i.e., i) global health monitoring, and ii) local health monitoring. In the latter category, ultrasonic-based SHM plays a crucial role in damage detection and localisation at the microscale. However, the accuracy and reliability of diagnosis are constricted by the quality of piezoelectric sensors. Under the operational condition, the sensor may deteriorate due to exposure to humidity, temperature fluctuations, and a corrosive environment. To avoid inaccuracies in the SHM framework, it is imperative to diagnose aberration to PZT sensors arising from surface defect, corrosion, and delamination [8], [9].

In the past few decades, a significant number of non-destructive evaluation (NDE) and SHM techniques have been

The associate editor coordinating the review of this manuscript and approving it for publication was Zihuai Lin[ID].

evolved and implemented for detecting the failure in critical structures [10]–[12]. Several non-destructive methodologies like; 1) neutron diffraction, 2) nano-indentation, 3) X-ray diffraction, and 4) Raman spectroscopy have been traditionally used to characterise PZT thin films [11], [12]. The above-mentioned techniques provide localised information on the mechanical properties of the material.

To enhance material characterisation and damage detection over a wide area, active sensing based on tuned Lamb waves and surface acoustic waves (SAWs) with piezoelectric wafers has been adapted due to its capability to propagate large distances without much loss of energy [3], [13]–[18]. These techniques being sensitive to defect are less appealing for high-resolution spatial localisation of surface and subsurface aberration.

To achieve high resolution acoustic imaging (∼1 MHz-1 GHz), Scanning Acoustic Microscopy (SAM) has evolved that utilises contrast in reflectivity of the elastic waves upon interaction with the surface defect [19], [20]. Rabe *et al.* [21] demonstrated the technique to measure the dynamic Young's Modulus at nanometer resolution on soft material using near field Atomic Force Acoustic Microscopy (AFAM). However, the technique is exclusive to measure surface properties and limits itself to quantify subsurface and bulk properties. Shilo *et al.* [22] has demonstrated high-resolution visualisation of high frequency (0.29 GHz) surface acoustic wave (SAWs) propagating in semiconductor crystal (Si and GaAs) without any additional electrode using X-ray diffraction. The novel approach has opened avenues for studying phonon interaction with a defect in piezo and non-piezoelectric crystal. However, the technique demands a high-intensity X-ray Synchrotron Radiation Facility that restricts its wide acceptability. Sugawara *et al.* [23], demonstrated visualisation of phonon vibrations with nano-meter resolution in the piezoelectric crystal using pico-second laser ultrasonic. The ultrashort optical pulse generates heat that creates non-equilibrium electron heating and spontaneous relaxation results in the generation of high frequency (∼1 GHz) strain waves. More recently, Scanning Laser Doppler Vibrometer (SLDV) has evolved to facilitate the three-dimensional visualisation of acoustic wave propagation in isotropic and anisotropic materials. Several studies have demonstrated the interference of guided waves with surface and subsurface inclusions in materials such as composite structures, piezoceramics, piezo-crystals, and metallic plate-like structures [24], [25]. However, both picosecond laser ultrasonic and SLDV, apart from being an expensive and time-consuming technique, required an optically opaque and polished sample surface.

Past one decade, our group has dedicated efforts to optimise the point contact excitation and detection method for the generation and visualisation of broadband ultrasonic waves in piezoelectric materials [26]–[31]. The technique has successfully demonstrated its diversity in excitation and detection of bulk and guided waves, metamorphosis to Lamb, and surface acoustic wave by exciting phonon vibration in piezoelectric

materials [26]–[32]. The phonon vibration is excited by virtue of transforming the electromagnetic field into mechanical energy [33]. A detailed description of the working principle, advantages over the other NDE of piezoelectric materials has already been published earlier and omitted herein [31], [32].

In order to excite and detect the ultrasonic waves, a probe made of a gold sphere or a steel sphere was used that acts as a Coulomb electrode. Habib *et al.* [30] have demonstrated the influence of probe radius on the directionality and forward contribution of the emitted and detected ultrasonic wave. This paper has extended the point contact excitation and detection technique to visualise the interaction of ultrasonic waves with a surface defect in sintered piezoceramic. The propagation of the ultrasonic wave in solid plate structures possesses a multiresolution characteristic of system dynamics. When the ultrasonic wave encounters the boundaries and defects, it continues to suffer from several reflections and interferences. Due to multiple interactions with edges and defects, often the ultrasonic waves undergo mode conversion resulting in spatial and temporal dispersion. In such a scenario, the localisation of defects from wave visualisation becomes challenging, in particular, when microscale and macroscale effects are conceivably differed in both space and time by orders of magnitude. Thus, it is essential to extract and quantify damage features from big-data.

We propose an advanced damage detection method based on multiresolution dynamic mode decomposition [34], image registration, and Kullback Leibler (KL) divergence [35]. The mrDMD algorithm is an extension of dynamic mode decomposition (DMD) with multiresolution analysis (MRA) in time. The mrDMD is ideally suited for the decomposition of complex waveforms and extract coherent spatiotemporal features. In a recent computer vision algorithm, DMD has been utilised to extract spatiotemporal features and applied to separate the foreground and background of video frames in real-time [36]. Bilal *et al.* [37] employed the mrDMD algorithm to detect the epileptic seizure. Further, Sikha and Soman [38] detected the salient region in noisy images by utilising the mrDMD algorithm. The well-suited methods to perform MRAs are windowed Fourier transform [39], Hilbert-Huang Transform [40] and wavelet-based methods [41], [42]. These techniques are limited in implementation in both space and time simultaneously. However, the mrDMD overcomes the limitation and separates the multiscale spatiotemporal features. To the best of our knowledge, none of these techniques in together or separately are employed for detection and localisation of damage.

The proposed damage detection algorithm has numerous advantages for high dimensional wave field images acquired by the Coulomb coupling technique. At the very outset, the data-driven and equation-free framework of the mrDMD algorithm reconstructs the underlying dynamics alone from the snapshot measurements [43]–[46]. Additionally, due to the strong connection between mrDMD and Koopman operator theory, the proposed technique is well suited to resolve the nonlinear and dispersive interaction of elastic waves with
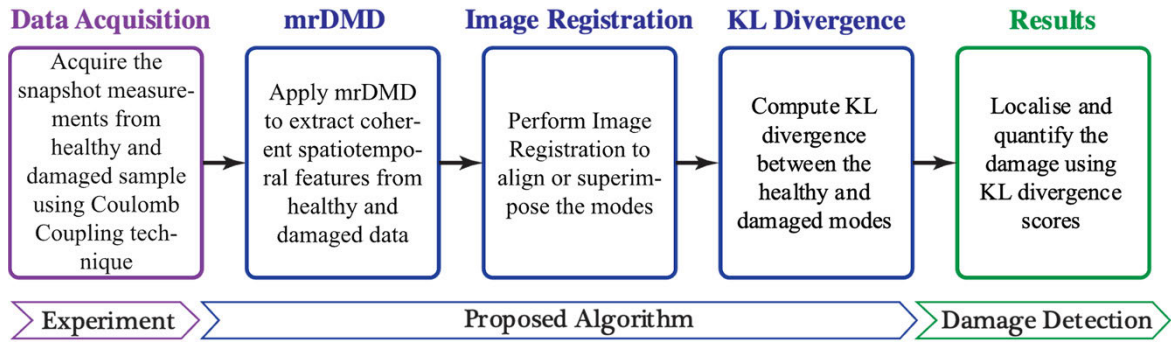
Data Acquisition	mrDMD	Image Registration	KL Divergence	Results
Acquire the snapshot measurements from healthy and damaged sample using Coulomb Coupling technique	Apply mrDMD to extract coherent spatiotemporal features from healthy and damaged data	Perform Image Registration to align or superimpose the modes	Compute KL divergence between the healthy and damaged modes	Localise and quantify the damage using KL divergence scores

Experiment | Proposed Algorithm | Damage Detection

FIGURE 1. Flowchart of the proposed novel damage detection algorithm.

boundaries and defects [47]–[50]. Finally, one can modify the DMD algorithm to take advantage of the sparse or limited measurement of the complex system [51], [52]. The experimental method based on the Coulomb Coupling technique is a well-suited method for the detection of surface cracks. Further, the proposed novel damage detection algorithm is a data-driven and equation-free technique. Recently data-driven breakthroughs are transforming how we detect,

model and control damages in the SHM framework. Most of the techniques available are based on empirical models or derivation based on first principles. In SHM, the systems depict as nonlinear, high-dimensional, dynamic, and multi-scale in space and time. With unprecedented accessibility of data and expanding computational resources make the novel data-driven algorithm robust and ease of use in real-life scenarios. The algorithm is divided into two-phase,
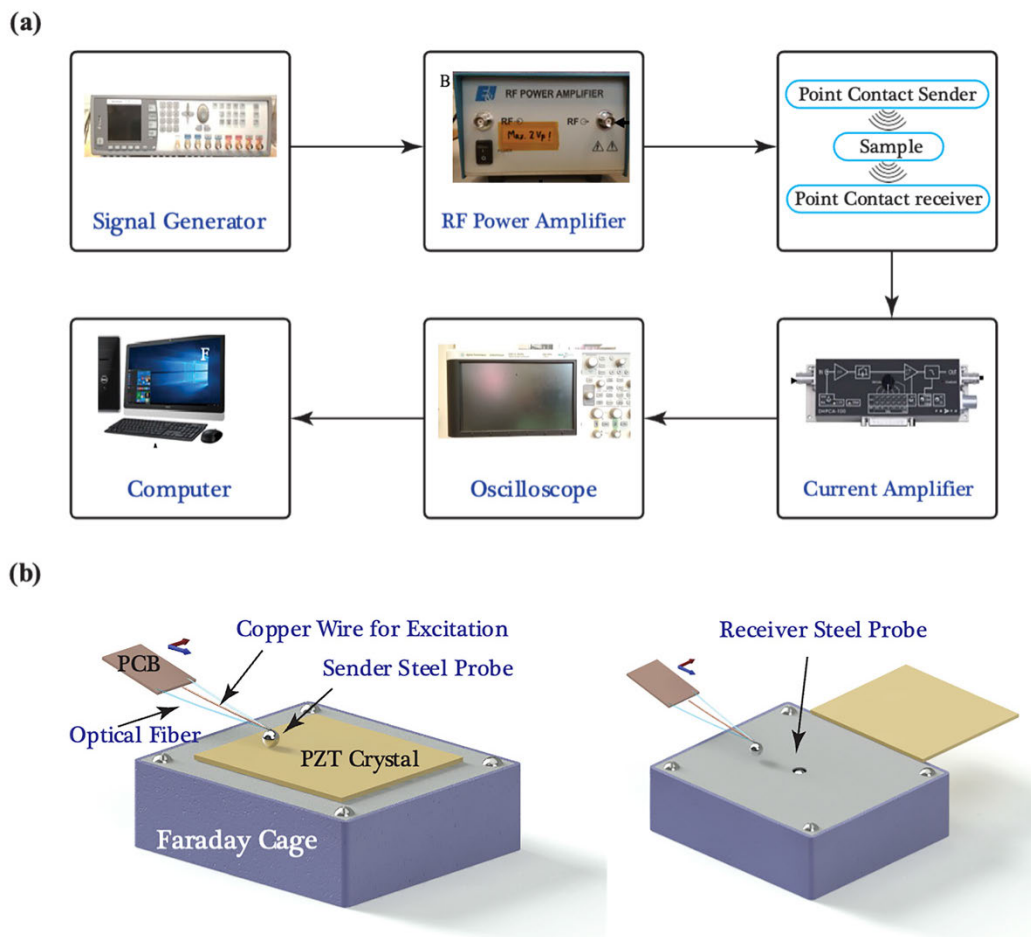
(a)

Signal Generator → RF Power Amplifier → Point Contact Sender / Sample / Point Contact receiver

Computer ← Oscilloscope ← Current Amplifier

(b)

Copper Wire for Excitation
Sender Steel Probe
PCB
Optical Fiber
PZT Crystal
Faraday Cage

Receiver Steel Probe

FIGURE 2. (a) Experimental setup for point contact excitation and detection scheme, and (b) 3D illustration of the arrangement of sender and receiver steel probe along with PZT.

i.e., i) spatiotemporal feature extraction using mrDMD, and ii) damage localisation using distance measure of the probability density of 2D wavefield image data-set of healthy state and damaged state. The advantages mentioned above of mrDMD combined with image registration and KL divergence mandate the developed data-driven algorithm as robust, accurate and computationally viable for the SHM framework. The schematic representation of the overview of the paper emphasising the damage-detection algorithm comprising of mrDMD, Image registration and KL divergence is shown in Fig. 1.

II. EXPERIMENTAL SETUP

Our group has previously provided a comprehensive overview of the excitation and detection probes fabrication, as well as the experimental setup [27], [29], [31], [32]. This innovative experimental technique for point contact excitation and detection is based on Coulomb coupling and is designed for the excitation and detection of ultrasonic waves in a piezoceramic. A Coulomb coupling technique is based on electro-mechanical excitation to generate an electric field that induces stress waves. The experimental method was designed for effective electric field coupling with elastic modulus and permittivity of piezoceramics. The experimental setup for point contact excitation and detection in PZT ceramic sample is depicted in Fig. 2.

The excitation Dirac delta pulse of 70 ns time width was produced using an arbitrary function generator (Agilent 81150A). The excited signal was routed to a radio-frequency (RF) amplifier (Electronics and Innovation: 403LA, New York, USA) for signal amplification. The amplified signal was sent to the excitation steel probe. The steel sphere made gentle contact with the sample's surface. The excited signal produced the acoustic waves in the PZT ceramic specimen. An identical steel sphere was employed on the opposite side of the PZT ceramic plate specimen to acquire the propagated signal, which was then amplified by a trans-impedance amplifier (DHPCA-100). A trans impedance amplifier of
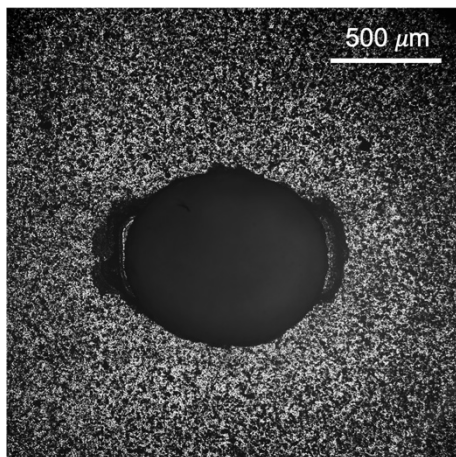

FIGURE 3. Optical image for the surface flaw of the PZT ceramic sample. The size of the defect is 1.2 mm × 1.3 mm and 1.5 mm in depth.

this kind transforms current into voltage using an adjustable amplification factor. Finally, the amplified signal was captured using an oscilloscope (Agilent 3024A) capable of digitising up-to 12 bits. The data collection sampling interval was 25 ns. The oscilloscope averages 256 pulse shots and digitises the signal, which is then saved in a personal computer (PC) via a USB port. The PC also controls the mechanical scanner in the XY plane, i.e., the step size is 50 μm in both directions and a scanning area of 10 mm × 10 mm.

The objective of the experiment was to visualise the wave propagation in the PZT sample and localise the defect in the sample. At first, a healthy PZT sample as a reference was placed in the experimental setup, and the measurement was performed. Following the completion of healthy state experiment, a calibrated damage was introduced on the surface of PZT ceramic with a high-speed diamond drill. The damage was approximately 1.2 mm × 1.3 mm and 1.5 mm in depth. The optical image of the drilled PZT can be seen in Fig. 3. The interaction of the ultrasonic wave with the damage was visualised by performing the experiment again.

III. MULTIRESOLUTION DYNAMIC MODE DECOMPOSITION (mrDMD)

To discuss the mathematical background of mrDMD, let us assume **S** be a matrix that represents a collection of two dimensional (2D) snapshots given in (1). The spatial dimension of each snapshot is $p \times q$, and there exists M number of such snapshots along the time axis. It is possible to unwrap each frame to a higher dimensional matrix, for instance, N − dimensional ($N = p \times q \gg 1$) column vector of a large data matrix **X**. Corresponding to each frame, the columns of **X** are sampled regularly at Δt in time as given in (2).

$$\mathbf{S} = \left[\mathbf{i}_{t_1}, \mathbf{i}_{t_2}, \ldots, \mathbf{i}_{t_M}\right]_{(p \times q) \times M} \qquad (1)$$

$$\mathbf{X} = [\mathbf{x}_1, \mathbf{x}_2, \ldots, \mathbf{x}_M]_{N \times M} \qquad (2)$$

To apply DMD, we can arrange the data matrix **X** into two matrices $\mathbf{X}_1$ and $\mathbf{X}_2$ as given in (3) and (4).

$$\mathbf{X}_1 = [\mathbf{x}_1, \mathbf{x}_2, \ldots, \mathbf{x}_{M-1}]_{N \times (M-1)} \qquad (3)$$

$$\mathbf{X}_2 = [\mathbf{x}_2, \mathbf{x}_3, \ldots, \mathbf{x}_M]_{N \times (M-1)} \qquad (4)$$

The DMD algorithm assumes that there exists a best-fit linear operator **F** relating both the $\mathbf{X}_1$ and $\mathbf{X}_2$ matrices as given in (5).

$$\mathbf{X}_2 = \mathbf{F}\mathbf{X}_1 \qquad (5)$$

where, **F** represents the system dynamics and is also referred to as the Koopman operator [34]. The matrix **F** can be computed by pseudo-inverse or eigen decomposition as given in (6).

$$\mathbf{F} = \mathbf{X}_2\mathbf{X}_1^{\dagger} \qquad (6)$$

where, † denotes Moore-Panrose pseudo inverse.

For a high dimensional data, i.e., N is large, the computation of matrix **F** may demand higher computational cost. To reduce the computational cost, the rank reduced representation of **F** as denoted by $\tilde{\mathbf{F}}$ is computed by projecting **F** onto proper orthogonal decomposition (POD) modes.

Further, to apply mrDMD, the samples of spatiotemporal data are selected such that all possible low and high-frequency contents are available. The mrDMD is a recursive approach of DMD, which extract the low-frequency features from the given spatiotemporal data. At first, the mrDMD removes m_1 modes and m_1 is the number of slow modes at level 1. The remaining modes are considered as the fast modes at level 1. Mathematically, mrDMD solution can be approximated as given in (7).

$$\mathbf{x}_{\mathrm{mrDMD}}(t) = \underbrace{\sum_{k=1}^{m_1} b_k(0)\,\phi_k^{(1)}(\xi)\exp(\omega_k t)}_{\text{(slow modes)}}$$
$$+ \underbrace{\sum_{k=m_1+1}^{M} b_k(0)\,\phi_k^{(1)}(\xi)\exp(\omega_k t)}_{\text{(fast modes)}} \quad (7)$$

where, ξ are the spatial coordinates, $b_k(0)$ is the initial amplitude of each mode. $\phi_k^{(1)}$ is DMD mode or eigenvector of full snapshot matrix, and $\exp(\omega_k t)$ is the corresponding eigenvalue. After the first level of decomposition, the time window is reduced for the second level. The DMD algorithm can be performed again with a reduced time window on the second sum, representing the fast modes of (7). However, the fast modes are again separated into two matrices.

$$\mathbf{X}_{M/2} = \mathbf{X}_{M/2}^{(1)} + \mathbf{X}_{M/2}^{(2)} \quad (8)$$

The first matrix of the right-hand side in (8) has the first $M/2$ snapshots, and the remaining snapshots are in the second matrix. At this level of decomposition, the m_2 slow-DMD modes are represented by $\phi_k^{(2)}$ are computed separately from the first- or second-time interval. This removal of slow modes is repeated recursively till the desired truncation level is achieved. This process is also represented
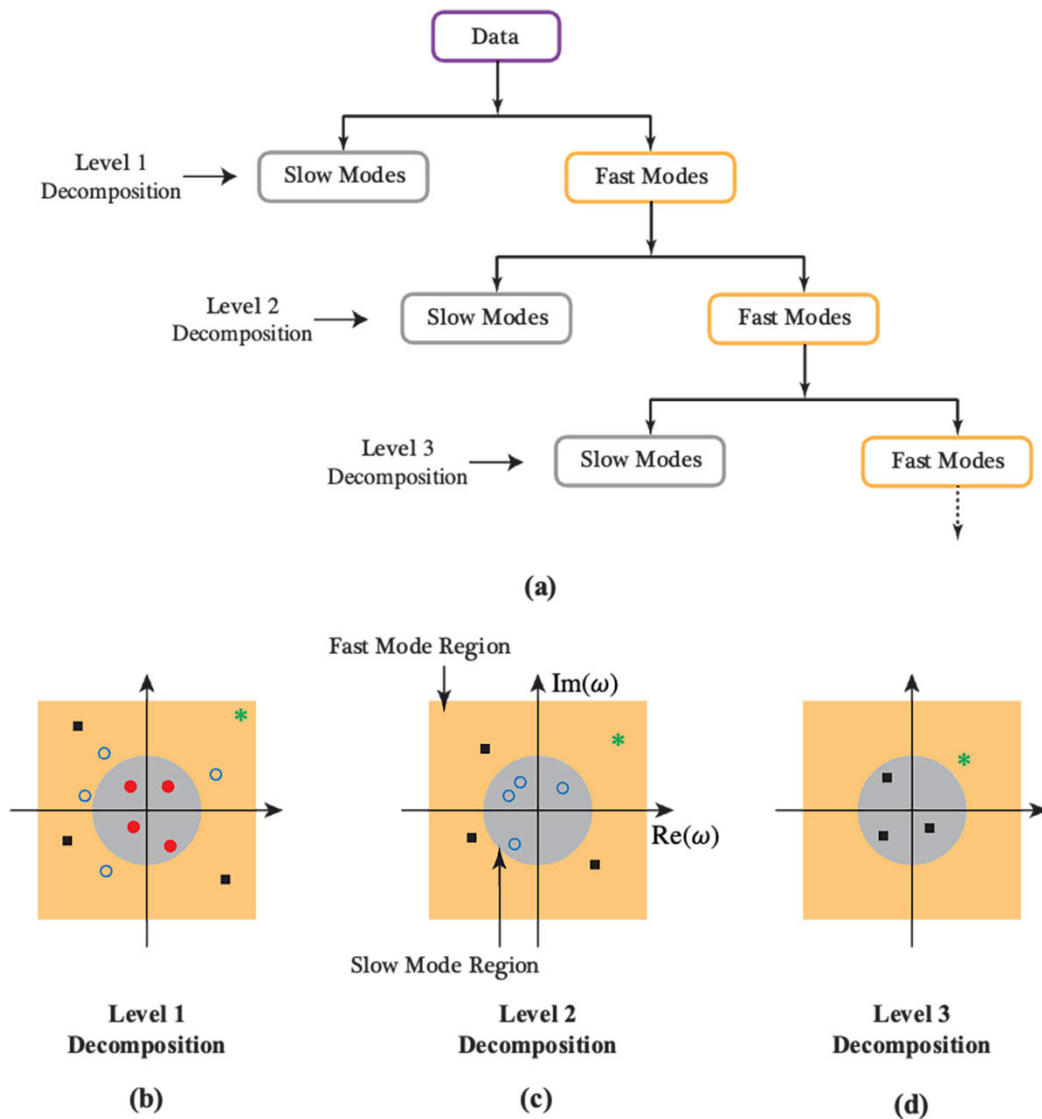

FIGURE 4. (a) The general structure of the mrDMD decomposition tree. Illustration of eigen value on a complex plane corresponding to the dynamic-modes at b) level 1, c) level 2, and d) level 3 of decomposition. The yellow and grey shaded regions represent slow and fast mode region at that level respectively.

in Fig. 4. The general mrDMD decomposition structure is illustrated in Fig. 4(a). The eigen value of (7) corresponding to a dynamic-mode represents a particular point on a complex plane. Referring to Fig. 4(b), Fig. 4(c) and Fig. 4(d), the slow dynamic-modes at a certain level of decomposition are represented by the points near to the origin of the complex plane. There exists m_1 slow modes at 1st level of decomposition which are shown by red dots on a complex plane in Fig. 4(b). The m_2 (blue circles) and m_3 (black squares) represent the slow dynamic-modes at 2nd and 3rd level of decomposition as shown in Fig. 4(c) and Fig. 4(d). The grey region illustrates the slow modes which are removed at that level. In Fig. 4(d), the green stars represent some dynamic-modes which can be extracted beyond 3rd level of decomposition.

The schematic diagram of the mrDMD technique is explained in Fig. 5. A three-level decomposition of mrDMD (left) and the sampling strategy of snapshots (right) at each level is shown in Fig. 5. The mrDMD extracts the slow varying features at level-1 (the bottom panel), and the fast scale features are successively extracted at a higher level of decomposition. The mrDMD method initially adapts M snapshots to capture slow scale features. At each higher level, successively, the sample size of the data is reduced to half of its previous level. The level 1 has the lowest frequencies of the dynamic-modes and increases as the level of decomposition an increase.

Formally, one can define the mrDMD solution in a generalised form as

$$\mathbf{x}_{\mathrm{mrDMD}}(t) = \sum_{l=1}^{L} \sum_{j=1}^{J} \sum_{k=1}^{m_L} f^{l,j}(t) b_k^{(l,j)} \phi_k^{(l,j)}(\xi) \exp(\omega_k^{(l,j)} t) \quad (9)$$

where,

$$l = 1, 2, \ldots, L : \text{number of decomposition levels}, \quad (10)$$

$$j = 1, 2, \ldots, J : \text{number of time bins per level}$$
$$(J = 2^{(l-1)}), \quad (11)$$

$$k = 1, 2, \ldots, m_L : \text{number of modes extracted}$$
$$\text{at level } L. \quad (12)$$

$f^{l,j}(t)$ is known as indicator function acts as a sifting function and is defined as:

$$f^{l,j}(t) = \begin{cases} 1, & t_j \leq t \leq t_{j+1} \\ 0, & elsewhere \end{cases} \quad (13)$$

Equation (9) represents the mrDMD solution containing the information about time bins, the number of decomposition levels and the modes extracted at various levels.

The detailed algorithm of mrDMD [34] is explained in brevity in the following section.

A. THE mrDMD ALGORITHM

Step 1: Construct the data matrices $\mathbf{X}_1$ and $\mathbf{X}_2$ at level l and time bin j of the decomposition as referred to in (3) and (4).

Step 2: Take the singular value decomposition (SVD) of $\mathbf{X}_1$

$$\mathbf{X}_1 = \mathbf{U}\boldsymbol{\Sigma}\mathbf{V}^* \quad (14)$$

where, $*$ denotes the conjugate transpose, $\mathbf{U} \in \mathbb{C}^{n \times r}$, $\boldsymbol{\Sigma} = \mathbb{C}^{r \times r}$, and $\mathbf{V} = \mathbb{C}^{m \times r}$. Here, r is the rank of the reduced SVD approximation to $\mathbf{X}_1$; the left singular vectors of $\mathbf{U}$ are POD modes.
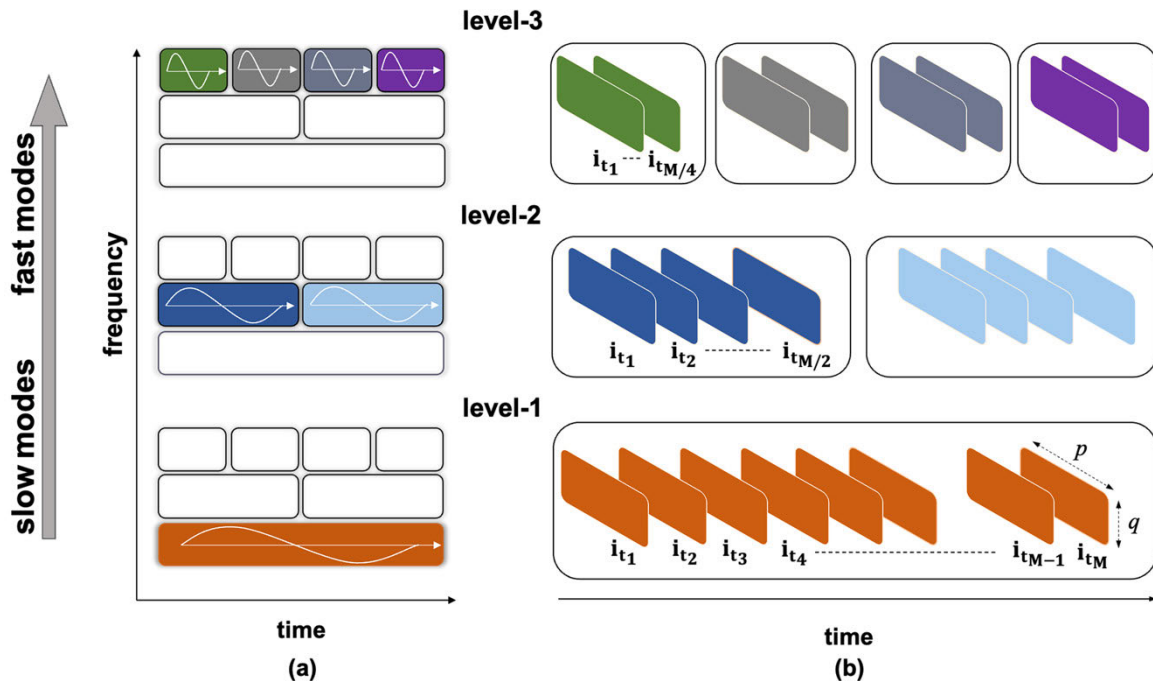

FIGURE 5. Illustration of mrDMD algorithm demonstrating sampling strategy of snapshots at various levels. a) time-frequency decomposition up to level-3 colour-coded with the snapshots, and b) snapshots of decomposition up to level-3 decomposition.

Step 3: Next, compute $\tilde{\mathbf{F}}^{(l,j)}$, the $r \times r$ projection of the entire matrix $\mathbf{F}^{(l,j)}$ onto POD modes:

$$\mathbf{F}^{(l,j)} = \mathbf{X}_2 \mathbf{V} \mathbf{\Sigma}^{-1} \mathbf{U}^*$$

$$\tilde{\mathbf{F}}^{(l,j)} = \mathbf{U}^* \mathbf{F}^{(l,j)} \mathbf{U} = \mathbf{U}^* \mathbf{X}_2 \mathbf{V} \mathbf{\Sigma}^{-1} \qquad (15)$$

Step 4: Compute the Eigen decomposition of $\tilde{\mathbf{F}}^{(l,j)}$

$$\tilde{\mathbf{F}}^{(l,j)} \mathbf{W} = \mathbf{W} \mathbf{\Lambda} \qquad (16)$$

where, the columns of $\mathbf{W}$ are eigenvectors and $\mathbf{\Lambda}$ is a diagonal matrix with the corresponding eigenvalues λ_k

Step 5: At this level of decomposition, collect the slow eigen values to construct slow modes, if present, where $\|\lambda_j\| < \rho$, and ρ is chosen in such a way to extract slow modes.

Step 6: Finally, reconstruct the Eigen decomposition of $\tilde{\mathbf{F}}^{(l,j)}$ from $\mathbf{W}$ and $\mathbf{\Lambda}$. Specifically, the eigen values of $\mathbf{F}^{(l,j)}$ are presented by $\mathbf{\Lambda}$, and the eigenvectors of $\mathbf{F}^{(l,j)}$ (DMD modes) are the same as the columns of $\mathbf{\Phi}^{(l,j)}$:

$$\mathbf{\Phi}^{(l,j)} = \mathbf{X}_2 \mathbf{V} \mathbf{\Sigma}^{-1} \mathbf{W} \qquad (17)$$

Step 7: Halve the initial sampling window at level $l + 1$, and repeat the procedure for each subsequent sample.

In step 2, the rank r may be chosen by the optimal hard threshold technique; the principled way of truncation is discussed briefly in the following section.

B. OPTIMAL HARD THRESHOLD TO OBTAIN SINGULAR VALUE TRUNCATION

Noise is an unavoidable part of data collected from an experiment. In such case, a principle way to truncate singular values of a data matrix $\mathbf{X}$ under the assumption that it has a low-rank matrix $\mathbf{X}_t$ with additive white noise error matrix $\mathbf{X}_n$ and noise magnitude υ is given by the recent theoretical discovery by Gavish and Donoho [53] that determines the optimal hard threshold τ:

$$\mathbf{X} = \mathbf{X}_t + \upsilon \mathbf{X}_n \qquad (18)$$

When the noise magnitude υ is known:

$$\tau = \eta \sqrt{N} \upsilon \qquad (19)$$

a. For a square matrix, $\mathbf{X} \in \mathbb{R}^{N \times N}$

$$\eta = \frac{4}{\sqrt{3}} \qquad (20)$$

b. For rectangular matrix, $\mathbf{X} \in \mathbb{R}^{N \times M}$ and $M \ll N$ with $\beta = M/N$

$$\eta(\beta) \triangleq \sqrt{2(\beta + 1) + \frac{8\beta}{(\beta + 1) + \sqrt{\beta^2 + 14\beta + 1}}} \qquad (21)$$

When the noise magnitude υ is unknown, this is usual in real-world situations:

a. For a rectangular matrix, $\mathbf{X} \in \mathbb{R}^{N \times M}$

$$\tau = \omega(\beta) \sigma_{med} \qquad (22)$$

Here, σ_{med} is the median singular value; $\omega(\beta) = \eta(\beta)/\mu_\beta$, μ_β can be approximated numerically by solving:

$$\int_{(1-\sqrt{\beta})^2}^{\mu_\beta} \frac{\sqrt{((1 + \sqrt{\beta})^2 - t)(t - (1 - \sqrt{\beta})^2)}}{2\pi t} dt = \frac{1}{2} \qquad (23)$$

The rank r of the reduced SVD approximation can be determined by using the technique as discussed in this section.

IV. IMAGE REGISTRATION

Image registration is the method of superimposing two or several images of the same event from various perspectives or sensors [54], [55]. With respect to the reference image, the sensed image is geometrically aligned. Image registration is utilised in the application where different way of image acquisition is considered such as a) Images of the same scene acquired from different viewpoints, b) Images of the same scene acquired at different times, c) Images of the same scene acquired by different sensors, and d) Scene to model registration. Universal method of image registration is not practical because of the variation of images and several types of degradation. The image registration should take into account factors such as geometric deformation among the images, required accuracy and the noise content. Nonetheless, registration methods mostly comprise of the following four steps [54] (see Fig. 6):

    a. Feature detection- Salient and distinctive features are manually or automatically detected.

    b. Feature matching- A spatial relationship among the detected features in the sensed image $v(x, y)$ and those in reference image $u(x, y)$ is established.

    c. Transform model estimation- The parameters of the mapping functions are computed with the help of established spatial relationship among the features.

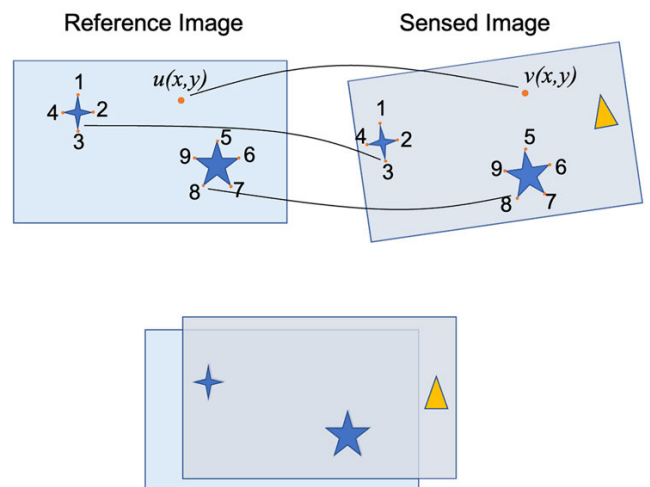   d. Image resampling and transformation- Mapping functions formed in the previous step are employed to

FIGURE 6. A schematic diagram representing the four steps of image registration.

transform the sensed image. The necessary interpolation technique is used to calculate image value in the co-ordinate where the information is missing after the transformation.

Finding the similarity is an important component in the proposed damage detection algorithm. An mrDMD mode from the healthy data is considered as a reference image and from the damage data is considered as a sensed image. After registering these images, they are compared based on the content. Here in this work, the author used KL divergence for comparison of the images. In the following section, the KL divergence is briefly discussed.

V. KL DIVERGENCE

The Kullback Leibler (KL) divergence measures the distance between the two probability density functions $h(x)$ and $u(x)$ [35]. In statistics, it characterises the entropy, and it is defined as:

$$D_{KL}(h \parallel u) \triangleq \int h(x) \log \frac{h(x)}{u(x)} dx \qquad (24)$$

KL divergence can be used efficiently to measure the similarity between images [56]. In information theory, it measures the information loss in the fitted model $u(x)$ relative to that in the reference model $h(x)$. Note that, $D_{KL}(h \parallel u) = 0$, if $h(x) = u(x)$ (since $\log 1 = 0$) which indicates the self-identification and $D_{KL}(h \parallel u) > 0$ for all $h(x)$ and $u(x)$.

VI. RESULTS AND DISCUSSIONS

In this section, we present results by implementing the proposed damage detection algorithm. Fig. 7 shows the visualisation of two dimension (2D) acoustic waves propagation in the PZT ceramic. The time interval of the 2D image is 190 ns. The total acquisition time of the temporal images was $1\mu s$,

corresponding to 365 time-varying snapshots. The dimension of the spatiotemporal data matrix **S** is $200 \times 200 \times 365$. Referring to Fig. 7 (H1-H2), the maximum intensity was observed at the centre of the image attributing to strong coupling of the electric-field. The outward radiating longitudinal wave generates circular wave fringe due to the isotropic property of the PZT ceramic.

Upon completion of the Coulomb scanning of the healthy specimen, a controlled surface damage was introduced in the PZT ceramic. The damaged ceramic was reoriented to ensure minimum scanning offset (translation/rotation) with respect to a healthy state. Fig. 8 shows the time-sequential images of wave propagation in damaged PZT ceramic. The surface defect in the PZT ceramic behaves as a reflector and impedes the transmission of the elastic wave. The forward propagating wave reflects from the surface defect and plate boundaries. The wave experience multiple interferences between the forward propagating and back-propagating reflected waves, as evident from Fig. 8 (D3-D6). Further, the interaction of ultrasonic wave with the defect cause attenuation of the bulk wave.

The precise detection and quantification of the defect directly from the experimental images are difficult due to the multiple interferences between the forward and reflected waves. To overcome the challenge, here we demonstrated an algorithm that separates spatiotemporal features emanating from the wave interaction with the defect. The main contribution of the paper is to develop a time-frequency based feature detection algorithm for damage detection and localisation of damage. The mrDMD is ideally suited for decomposition of complex waveform and extract spatiotemporal features of damage. The algorithm is divided in two phases i.e., i.) spatiotemporal feature extract using mrDMD, and ii) damage localisation using distance measure of probability
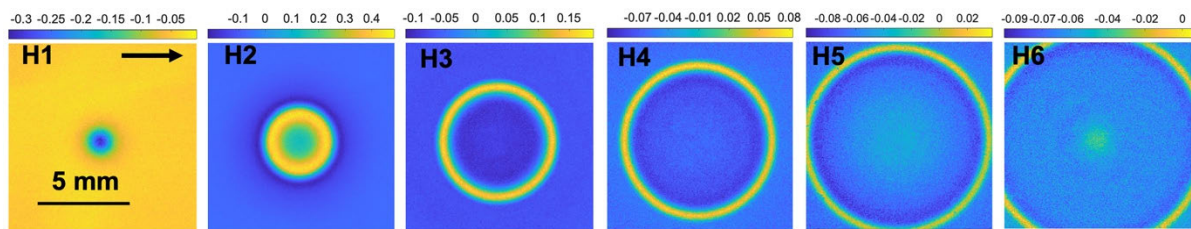

FIGURE 7. The sequential images of propagation of acoustic wave at an interval of 190 ns in a 3 mm thick sintered PZT ceramic plate (healthy state). The scanning region was 10 mm × 10 mm.
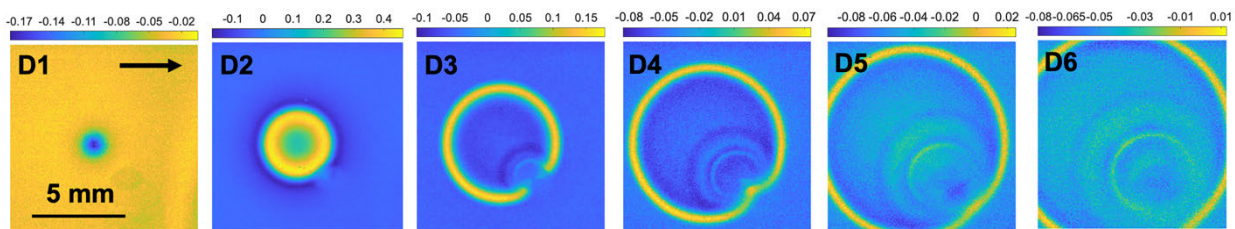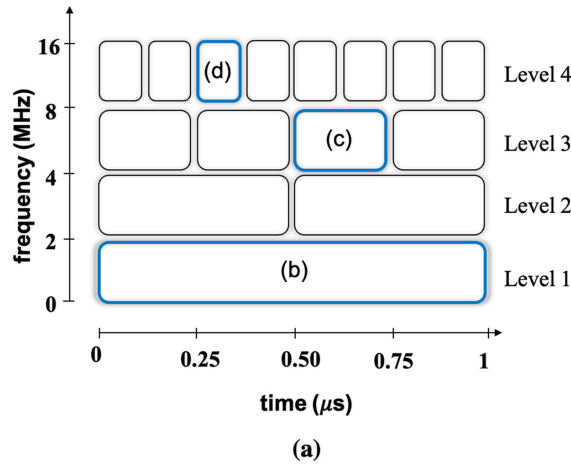

FIGURE 8. The sequential images of propagation of acoustic wave at an interval of 190 ns in a 3 mm thick sintered PZT ceramic plate (with surface defect). The scanning region was 10 mm × 10 mm.

4-level decomposition

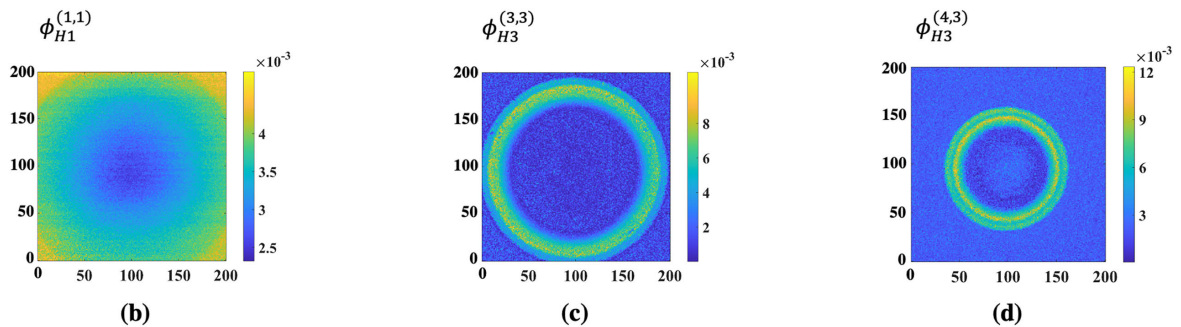**mrDMD modes in healthy state**

FIGURE 9. Results of mrDMD applied on 2D wave propagation in healthy PZT ceramic. a) Four-level of time frequency decomposition (top panel), b) level 1, c) level 3, and d) level 4 of mrDMD modes (bottom panel).

density of 2D wave field image dataset of healthy state and damaged state.

Fig. 9 and Fig. 10 represent the results obtained by applying the mrDMD algorithm in the healthy and damaged state, respectively [34], [57]. Fig. 9(b) and Fig. 10(b) shows first level of decomposition, representing slowest wave mode for healthy and damaged state, respectively. Refer to Fig. 9(b) and Fig. 10(b), the slowest wave mode is denoted by $\phi_{H1}^{(1,1)}$ and $\phi_{D1}^{(1,1)}$ that represent the long time period. In this mode, the strong intensity at the centre is observed due to the strong coupling of the electric field. Fig. 9(c) and Fig. 9(d) represent level 3 and level 4 of mrDMD modal decomposition for healthy sample. The higher-order modes represent fast-varying features of acoustic wave propagation in PZT that are sensitive to surface and subsurface defects.

The data-driven approach of mrDMD extracts sensitive spatiotemporal features of the wave interaction with the defect. Fig. 10 shows the four-level of mrDMD decomposition of spatiotemporal wavefield imaging in the defective PZT. Further, at the first level of decomposition, the extracted mode, $\phi_{D1}^{(1,1)}$, of the damaged state shows the impression of the surface defect (Fig. 10 (b)). However, the lowest order

mode has long wavelength that restricts the spatial resolution. The level-3, $\phi_{D3}^{(3,3)}$ of mrDMD decomposition, shows extracted feature of the reflected wave from the edge of the defect along with the forward propagating acoustic waves (Fig. 10(c)). Further, Fig. 10(d) illustrates the mrDMD level 3 mode, $\phi_{D4}^{(3,3)}$ that shows considerably low intensity of the reflected wave. Upon, comparison of the original wavefield image, (refer Fig. 8-D3), with level-3 mrDMD mode shows a similar observation of reduced intensity. For both healthy and damaged situation, a 4-level decomposition is sufficient to extract spatiotemporal sensitive features.

Considering, the decomposition of mrDMD modes, the subsequent objective is to localise and quantify the damage in the PZT. To achieve this, we considered the slowest mode, $\phi_{H1}^{(1,1)}$ and $\phi_{D1}^{(1,1)}$ at level 1 of the decomposition from both the healthy and damaged data. Since, the healthy and damaged data are disjoint and acquired independently, hence, it is presumed that the 2D wave filed image will possess geometrical offset and rotation. As, the mrDMD modes are extracted from raw images, the offset or rotation will also present in such modes. A minor offset or rotation can lead to a considerable error in the quantification of the defect.

4-level decomposition

(a)
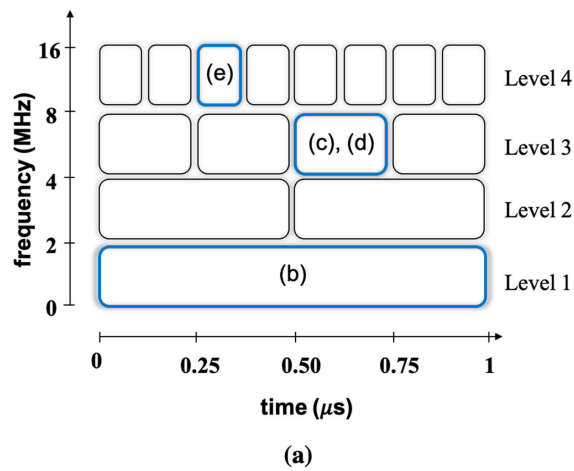
mrDMD modes in damaged state

(b)   **(c)**   **(d)**   **(e)**
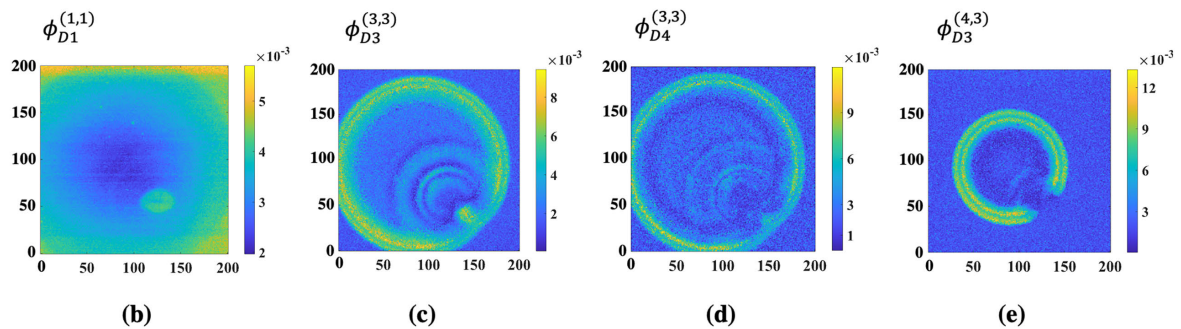
FIGURE 10. Results of mrDMD applied on 2D wave propagation in damage PZT ceramic. a) Four-level of time frequency decomposition (top panel), b) level 1, c) and d) level 3, and e) level 4 of mrDMD modes (bottom panel).
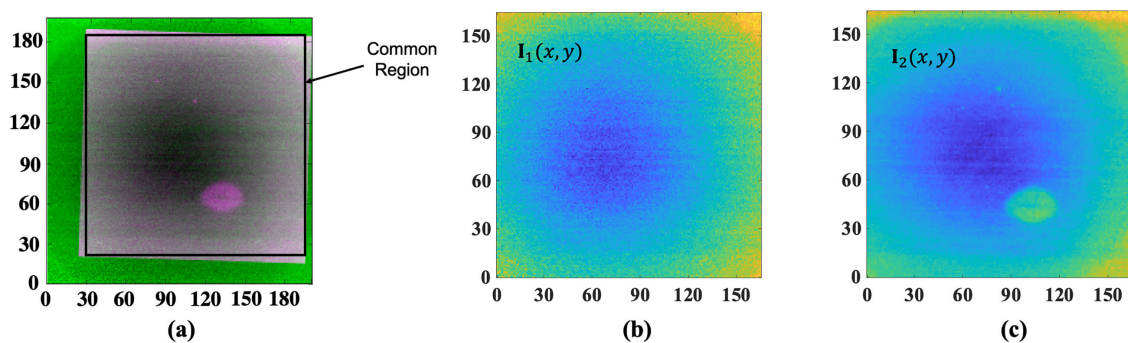

(a)   **(b)**   **(c)**

FIGURE 11. Results of intensity-based image registration. a) The damage mode (magenta) is registered and overlaid on the healthy mode (green), b) the aligned cropped image of healthy mode, and c) the aligned cropped image of damage mode.

To overcome the errors arising due to offset in the considered modes, the intensity-based image registration technique is employed. In the intensity-based image registration, the healthy mode is considered as a reference image (green) and the damage mode as translated/rotated image (magenta) (refer to Fig. 11(a)). Fig. 11 shows the outcome of offset correction obtained through the image registration technique.

The common region of Fig. 11(a) is selected and masked for quantifying the defect. Fig. 11(b) and Fig. 11(c) show the resulting aligned cropped images for healthy and damaged mode, respectively.

Once the process of image registration is performed, the localisation and quantification of damage are performed by computing the KL divergence. The key idea of computing
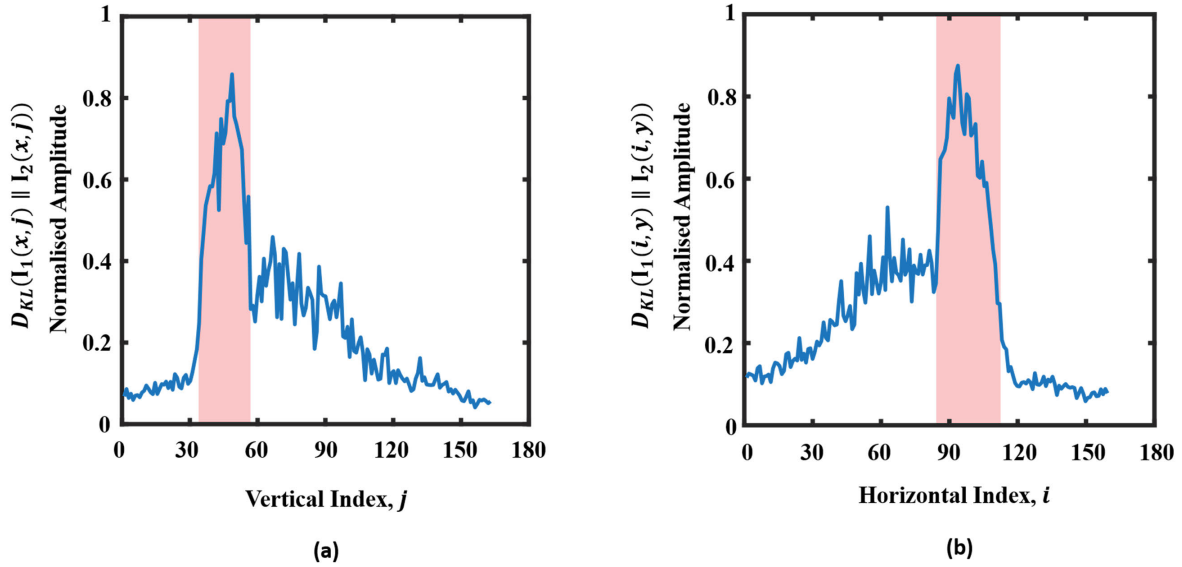
FIGURE 12. Plot of normalized KL Divergence scores. a) The scores are computed by first considering the horizontal strip and sliding across along the vertical direction, and b) the vertical strip sliding across along the horizontal direction.

KL divergence is computing the statistical distance between the modes of healthy and damaged states. The mrDMD mode of damage state almost exhibits the mode of healthy state with some loss of information at the damage location. Consider $I_1(x, y)$ and $I_2(x, y)$ represent the output masked image of the healthy and damaged state respectively; the dimension of each image is $w \times h$. As discussed in section V, KL divergence scores are minimum for similar modes (i.e $I_1(x, y) \approx I_2(x, y)$). Here, we computed KL divergence strip-wise; first a horizontal strip is considered and sliding the strip along the vertical direction ($I_k(x, j); 1 \leq k \leq 2; 1 \leq j \leq h$) and vice

versa ($I_k(i, y); 1 \leq k \leq 2; 1 \leq i \leq w$). The computation of KL divergence scores by considering both directions are illustrated in Fig. 12.

Referring to Fig. 12(a), sliding strip along the vertical direction, the KL divergence scores suddenly escalate in the domain from $j = 34$ to $j = 56$. Similarly, from Fig. 12(b), the strip along the horizontal direction, in the domain from $i = 87$ to $i = 116$ the KL divergence scores are again increased abruptly. Referring to Fig. 13, a rectangular region is compartmentalised between $j = 34$ to 56 and $i = 87$ to 116 which conforms to the location of the defect. The size of the surface flaw is quantified approximately 1.1 mm $\times$ 1.4 mm. The original size of the defect was approximately 1.2 mm $\times$ 1.3 mm. Therefore, the proposed algorithm is efficient for localisation and quantification of the damage with an error of about 1.3%.

Further, we implemented the algorithm repeatedly by varying several parameters to illustrate the reliability of the proposed algorithm. The first parameter considered here is the rank r that has significant importance in the mrDMD algorithm. It depends on the factors such as the amount of noise and the distribution of the singular values. Often, one selects the rank r of the SVD by identifying "elbows" or "knees" in the plots of singular values on the logarithmic scale. The "elbows" or "knees" may represent the transition of important patterns from noise. Another way of truncating the singular values at the rank r that captures a pre-defined energy such as 80% or 90% in the original data [57]. Despite primitive, these techniques are commonly used. To overcome this, a principled approach to obtaining rank reduced SVD is discussed in Section III-B. We also implemented the algorithm by setting the rank r on identifying the "elbows" from the distribution of singular values in a logarithmic scale. The
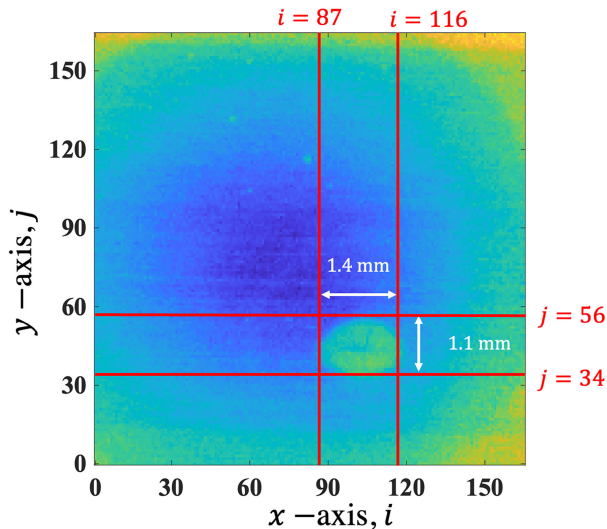

FIGURE 13. Localisation of the surface defect in a rectangular region between $i = 87$ to 116 and $j = 34$ to 56 unit. The size of the surface defect is quantified as approximately 1.4 mm $\times$ 1.1 mm.

damage is identified with an accuracy of about 97%. As stated earlier, the accuracy is further improved when the optimal truncation value is employed using the optimal hard threshold technique as discussed in Section III-B. The second parameter considered to illustrate the reliability is ρ in step 5 of the mrDMD algorithm. The parameter ρ is chosen to extract slow modes. There is some liberty in the selection of ρ. This value is selected based on the length of the sampling window. The results presented in this paper chooses the value of ρ in such a way that to extract modes with fewer than two cycles within the sampling window. However, the algorithm is repeated by setting the various values of ρ, such as one cycle and three cycles of oscillations. In each repetition, the damage is identified with an error of less than 5%. Finally, defining the limits of the escalating region in the plot of the KL divergence score is a contentious choice. However, one can define the limit by threshold crossing of the KL divergence score.

VII. CONCLUSION

Multiresolution dynamic mode decomposition is an equation-free data-driven technique that explores the underlying system dynamics by extracting spatiotemporal coherent mode. The unique ability of mrDMD is leveraged to extract higher-order dynamic-modes of the ultrasonic wave. The point source technique based on Coulomb coupling is employed for the excitation and detection of ultrasonic waves in PZT sensors. The two-dimensional spatial temporal evolution of waves in the PZT is imaged for diagnosis and localisation of surface defects in the PZT. The mrDMD provides input-output models for the interaction of waves with complex geometries. The coherent mode of propagation of elastic waves are filtered, and modes sensitive to defect are considered for localisation. Further, KL divergence method in two-dimensional scanning mode is used to localise the detects from the mrDMD defect sensitive modes. The proposed algorithm exhibits good accuracy in detecting and quantifying damage with an error of around 1.3%. Albeit, the technique being implemented on full-field transient imaging, has still poised itself to perform satisfactorily in situations of data sparsity that needs further investigation.

REFERENCES

[1] S. Bhalla and C. K. Soh, "Structural health monitoring by piezo-impedance transducers. I: Modeling," *J. Aerosp. Eng.*, vol. 17, no. 4, pp. 154–165, Oct. 2004.

[2] C. P. Providakis, K. D. Stefanaki, M. E. Voutetaki, Y. Tsompanakis, and M. Stavroulaki, "Damage detection in concrete structures using a simultaneously activated multi-mode PZT active sensing system: Numerical modelling," *Struct. Infrastruct. Eng.*, vol. 10, no. 11, pp. 1451–1468, Nov. 2014.

[3] A. Shelke, T. Kundu, U. Amjad, K. Hahn, and W. Grill, "Mode-selective excitation and detection of ultrasonic guided waves for delamination detection in laminated aluminum plates," *IEEE Trans. Ultrason., Ferroelectr., Freq. Control*, vol. 58, no. 3, pp. 567–577, Mar. 2011.

[4] K. K. Shung, *Diagnostic Ultrasound: Imaging and Blood Flow Measurements*. Boca Raton, FL, USA: CRC Press, 2015.

[5] G. T. Hwang, V. Annapureddy, J. H. Han, D. J. Joe, C. Baek, D. Y. Park, D. H. Kim, J. H. Park, C. K. Jeong, K. I. Park, and J. J. Choi, "Self-powered wireless sensor node enabled by an aerosol-deposited PZT flexible energy harvester," *Adv. Energy Mater.*, vol. 6, no. 13, 2016, Art. no. 1600237.

[6] C. R. Farrar and N. A. J. Lieven, "Damage prognosis: The future of structural health monitoring," *Philos. Trans. Roy. Soc. A, Math., Phys. Eng. Sci.*, vol. 365, no. 1851, pp. 623–632, 2007.

[7] L. Hui and O. Jinping, "Structural health monitoring: From sensing technology stepping to health diagnosis," *Procedia Eng.*, vol. 14, pp. 753–760, Jan. 2011.

[8] J. M. W. Brownjohn, "Structural health monitoring of civil infrastructure," *Philos. Trans. Roy. Soc. A*, vol. 365, no. 1851, pp. 589–622, 2007.

[9] C. R. Farrar, K. Worden, N. A. Lieven, and G. Park, "Nondestructive evaluation of structures," in *Encyclopedia of Aerospace Engineering*. Hoboken, NJ, USA: Wiley, 2010, doi: 10.1002/9780470686652.eae186.

[10] M. Todd, J. Nichols, L. Pecora, and L. Virgin, "Vibration-based damage assessment utilizing state space geometry changes: Local attractor variance ratio," *Smart Mater. Struct.*, vol. 10, no. 5, p. 1000, 2001.

[11] M. D. Duncan, M. Bashkansky, and J. Reintjes, "Subsurface defect detection in materials using optical coherence tomography," *Opt. Exp.*, vol. 2, pp. 540–545, Jun. 1998.

[12] S. T. Quek, P. S. Tua, and J. Jin, "Comparison of plain piezoceramics and inter-digital transducer for crack detection in plates," *J. Intell. Mater. Syst. Struct.*, vol. 18, no. 9, pp. 949–961, Sep. 2007.

[13] J. L. Rose and P. B. Nagy, "Ultrasonic waves in solid media," *J. Acoust. Soc. Amer.*, vol. 107, no. 4, pp. 1807–1808, 2000.

[14] T. Kundu, *Ultrasonic Nondestructive Evaluation: Engineering and Biological Material Characterization*. Boca Raton, FL, USA: CRC Press, 2003.

[15] V. Giurgiutiu, *Structural Health Monitoring: With Piezoelectric Wafer Active Sensors*. Amsterdam, The Netherlands: Elsevier, 2007.

[16] T. Kundu, F. L. di Scalea, and H. Sohn, "Special section guest editorial: Structural health monitoring: Use of guided waves and/or nonlinear acoustic techniques," *Opt. Eng.*, vol. 55, no. 1, Dec. 2015, Art. no. 011001.

[17] T. Kundu and A. K. Mal, "Diffraction of elastic waves by a surface crack on a plate," *J. Appl. Mech.*, vol. 48, no. 3, pp. 570–576, Sep. 1981.

[18] L. Pamwani, A. Habib, F. Melandsø, B. S. Ahluwalia, and A. Shelke, "Single-input and multiple-output surface acoustic wave sensing for damage quantification in piezoelectric sensors," *Sensors*, vol. 18, no. 7, p. 2017, Jun. 2018.

[19] A. Habib, A. Shelke, M. Vogel, S. Brand, X. Jiang, U. Pietsch, S. Banerjee, and T. Kundu, "Quantitative ultrasonic characterization of c-axis oriented polycrystalline AlN thin film for smart device application," *Acta Acustica United Acustica*, vol. 101, no. 4, pp. 675–683, Jul. 2015.

[20] A. Habib, A. Shelke, M. Vogel, U. Pietsch, X. Jiang, and T. Kundu, "Mechanical characterization of sintered piezo-electric ceramic material using scanning acoustic microscope," *Ultrasonics*, vol. 52, no. 8, pp. 989–995, Dec. 2012.

[21] U. Rabe, S. Amelio, M. Kopycinska, S. Hirsekorn, M. Kempf, M. Göken, and W. Arnold, "Imaging and measurement of local mechanical material properties by atomic force acoustic microscopy," *Surf. Interface Anal.*, vol. 33, no. 2, pp. 65–70, Feb. 2002.

[22] D. Shilo, E. Lakin, E. Zolotoyabko, J. Härtwig, and J. Baruchel, "X-ray imaging of surface acoustic waves generated in semiconductor crystals by an external transducer," *Appl. Phys. Lett.*, vol. 82, no. 9, pp. 1374–1376, Mar. 2003.

[23] Y. Sugawara, O. B. Wright, O. Matsuda, M. Takigahira, Y. Tanaka, S. Tamura, and V. E. Gusev, "Watching ripples on crystals," *Phys. Rev. Lett.*, vol. 88, no. 18, Apr. 2002, Art. no. 185504.

[24] A. K. Kromine, "Detection of subsurface defects using laser based technique," in *Proc. AIP Conf.*, 2001, vol. 557, no. 1, pp. 1612–1617.

[25] Z. Wang, W. Zhu, H. Zhu, J. Miao, C. Chao, C. Zhao, and O. K. Tan, "Fabrication and characterization of piezoelectric micromachined ultrasonic transducers with thick composite PZT films," *IEEE Trans. Ultrason., Ferroelectr., Freq. Control*, vol. 52, no. 12, pp. 2289–2297, Dec. 2005.

[26] A. Shelke, A. Habib, U. Amjad, M. Pluta, T. Kundu, U. Pietsch, and W. Grill, "Metamorphosis of bulk waves to Lamb waves in anisotropic piezoelectric crystals," *Health Monitor. Struct. Biol. Syst.*, vol. 7984, 2011, Art. no. 798415.

[27] A. Habib, E. Twerdowski, M. von Buttlar, M. Pluta, M. Schmachtl, R. Wannemacher, and W. Grill, "Acoustic holography of piezoelectric materials by Coulomb excitation," *Health Monitor. Smart Nondestruct. Eval. Struct. Biol. Syst. V*, vol. 6177, Mar. 2006, Art. no. 61771A.

[28] G. Tripathi, H. Anowarul, K. Agarwal, and D. Prasad, "Classification of micro-damage in piezoelectric ceramics using machine learning of ultrasound signals," *Sensors*, vol. 19, no. 19, p. 4216, Sep. 2019.

[29] A. Habib, U. Amjad, M. Pluta, U. Pietsch, and W. Grill, "Surface acoustic wave generation and detection by Coulomb excitation," *Health Monitor. Struct. Biol. Syst.*, vol. 7650, Apr. 2010, Art. no. 76501T.

[30] A. Habib, E. Twerdowski, M. von Buttlar, R. Wannemacher, and W. Grill, "The influence of the radius of the electrodes employed in Coulomb excitation of acoustic waves in piezoelectric materials," *Health Monitor. Struct. Biol. Syst.*, vol. 6532, Apr. 2007, Art. no. 653214.

[31] A. Habib, A. Shelke, M. Pluta, T. Kundu, U. Pietsch, and W. Grill, "Imaging of acoustic waves in piezoelectric ceramics by Coulomb coupling," *Jpn. J. Appl. Phys.*, vol. 51, no. 7S, 2012, Art. no. 07GB05.

[32] V. Agarwal, A. Shelke, B. S. Ahluwalia, F. Melandsø, T. Kundu, and A. Habib, "Damage localization in piezo-ceramic using ultrasonic waves excited by dual point contact excitation and detection scheme," *Ultrasonics*, vol. 108, Dec. 2020, Art. no. 106113.

[33] A. Habib, A. Shelke, M. Pluta, U. Pietsch, T. Kundu, and W. Grill, "Scattering and attenuation of surface acoustic waves and surface skimming longitudinal polarized bulk waves imaged by Coulomb coupling," in *Proc. AIP Conf.*, 2012, vol. 1433, no. 1, pp. 247–250.

[34] J. N. Kutz, X. Fu, and S. L. Brunton, "Multiresolution dynamic mode decomposition," *SIAM J. Appl. Dyn. Syst.*, vol. 15, no. 2, pp. 713–735, 2016.

[35] S. Kullback and R. A. Leibler, "On information and sufficiency," *Ann. Math. Statist.*, vol. 22, no. 1, pp. 79–86, 1951.

[36] J. N. Kutz, J. Grosek, and S. L. Brunton, "Dynamic mode decomposition for robust pca with applications to foreground/background subtraction in video streams and multi-resolution analysis," in *Handbook on Robust Low-Rank and Sparse Matrix Decomposition: Applications in Image and Video Processing*. Boca Raton, FL, USA: CRC Press, 2016, ch. 19.

[37] M. Bilal, M. Rizwan, S. Saleem, M. M. Khan, M. S. Alkatheir, and M. Alqarni, "Automatic seizure detection using multi-resolution dynamic mode decomposition," *IEEE Access*, vol. 7, pp. 61180–61194, 2019.

[38] O. K. Sikha and K. P. Soman, "Multi-resolution dynamic mode decomposition-based salient region detection in noisy images," *Signal, Image Video Process.*, vol. 14, no. 1, pp. 167–175, Feb. 2020.

[39] J. N. Kutz, *Data-Driven Modeling & Scientific Computation: Methods for Complex Systems & Big Data*. New York, NY, USA: Oxford Univ. Press, 2013.

[40] N. E. Huang, *Hilbert-Huang Transform and its Applications*. Singapore: World Scientific, 2014.

[41] I. Daubechies, *Ten Lectures on Wavelets*. Philadelphia, PA, USA: SIAM, 1992.

[42] L. Debnath and F. A. Shah, *Wavelet Transforms and Their Applications*. Cambridge, MA, USA: Springer, 2002.

[43] K. K. Chen, J. H. Tu, and C. W. Rowley, "Variants of dynamic mode decomposition: Boundary condition, Koopman, and Fourier analyses," *J. Nonlinear Sci.*, vol. 22, no. 6, pp. 887–915, Mar. 2012.

[44] P. J. Schmid, "Dynamic mode decomposition of numerical and experimental data," *J. Fluid Mech.*, vol. 656, pp. 5–28, Jan. 2010.

[45] P. J. Schmid, K. E. Meyer, and O. Pust, "Dynamic mode decomposition and proper orthogonal decomposition of flow in a lid-driven cylindrical cavity," in *Proc. 8th Int. Symp. Part. Image Velocimetry*, 2009, pp. 25–28.

[46] J. H. Tu, C. W. Rowley, D. M. Luchtenburg, S. L. Brunton, and J. N. Kutz, "On dynamic mode decomposition: Theory and applications," 2013, *arXiv:1312.0041*. [Online]. Available: http://arxiv.org/abs/1312.0041

[47] M. Budišić, R. Mohr, and I. Mezić, "Applied koopmanism," *Chaos: Interdiscipl. J. Nonlinear Sci.*, vol. 22, no. 4, Dec. 2012, Art. no. 047510.

[48] B. O. Koopman, "Hamiltonian systems and transformation in Hilbert space," *Proc. Nat. Acad. Sci. USA*, vol. 17, no. 5, p. 315, 1931.

[49] I. Mezić, "Analysis of fluid flows via spectral properties of the Koopman operator," *Annu. Rev. Fluid Mech.*, vol. 45, no. 1, pp. 357–378, Jan. 2013.

[50] C. W. Rowley, I. Mezić, S. Bagheri, P. Schlatter, and D. S. Henningson, "Spectral analysis of nonlinear flows," *J. Fluid Mech.*, vol. 641, pp. 115–127, Dec. 2009.

[51] S. L. Brunton, J. L. Proctor, and J. N. Kutz, "Compressive sampling and dynamic mode decomposition," 2013, *arXiv:1312.5186*. [Online]. Available: http://arxiv.org/abs/1312.5186

[52] M. R. Jovanović, P. J. Schmid, and J. W. Nichols, "Sparsity-promoting dynamic mode decomposition," *Phys. Fluids*, vol. 26, no. 2, Feb. 2014, Art. no. 024103.

[53] M. Gavish and D. L. Donoho, "The optimal hard threshold for singular values is $4/\sqrt{3}$," *IEEE Trans. Inf. Theory*, vol. 60, no. 8, pp. 5040–5053, Aug. 2014.

[54] B. Zitová and J. Flusser, "Image registration methods: A survey," *Image Vis. Comput.*, vol. 21, pp. 977–1000, Oct. 2003.

[55] L. G. Brown, "A survey of image registration techniques," *ACM Comput. Surv.*, vol. 24, no. 4, pp. 325–376, Dec. 1992.

[56] J. Goldberger, S. Gordon, and H. Greenspan, "An efficient image similarity measure based on approximations of KL-divergence between two Gaussian mixtures," in *Proc. ICCV*, vol. 3, 2003, pp. 487–493.

[57] J. N. Kutz, S. L. Brunton, B. W. Brunton, and J. L. Proctor, *Dynamic Mode Decomposition: Data-Driven Modeling of Complex Systems*. Philadelphia, PA, USA: SIAM, 2016.

NUR M. M. KALIMULLAH received the B.Tech. degree in civil engineering from North Eastern Regional Institute of Science and Technology, in 2018. He is currently pursuing the Ph.D. degree with Indian Institute of Technology Guwahati. His research interests include structural health monitoring and wave propagation.

AMIT SHELKE received the B.S. degree in civil engineering from the National Institute of Technology, in 2005, the M.S. degree from Indian Institute of Technology Kanpur, in 2007, and the Ph.D. degree from the University of Arizona, Tucson, AZ, USA, in 2011. He is currently an Associate Professor with Indian Institute of Technology Guwahati. His research interests include wave propagation, nondestructive evaluation, and structural health monitoring.

ANOWARUL HABIB received the M.Sc. degree in physics from the University of Leipzig, Germany, in 2006, and the Ph.D. degree in ultrasonics from the University of Siegen, Germany, in 2013. After Ph.D., he worked as a Postdoctoral Fellow with Goethe University Frankfurt. Later on, he joined UiT The Arctic University of Norway as a Senior Research Fellow. His main research interests include the development of scanning acoustic microscopy, point contact excitation and detection methods, high-frequency polymer transducer fabrication, and structural health monitoring. In 2011, he was awarded the Best Young Scientist Award from Symposium on Ultrasonic Electronics, Japan.

• • •